

## About the Formation of Macrosegregations During Continuous Casting of Sn-Bronze

A. Ludwig<sup>1,2</sup>, M. Gruber-Pretzler<sup>2</sup>, M. Wu<sup>2</sup>, A. Kuhn<sup>3</sup>, J. Riedle<sup>3</sup>

In continuous casting of bronze, macrosegregations cause weaknesses in the final product. Besides sedimentation and flotation of equiaxed grains, feeding flow, thermal and solutal buoyancy driven flow, and inlet flow are potential convection mechanisms which cause the formation of macrosegregations. Since macrosegregations are formed during solidification processes where relative motion between melt and solidifying dendrites occurs, their formation is strongly dependent on the flow, especially in the mushy zone. To study and compare the impact of the different flow phenomena, a numerical investigation has been carried out. The presented study discusses the impact of different convection types like inlet flow, thermal and solutal buoyancy flow, and feeding flow on the formation of macrosegregations for one highly and one low permeable mushy zone. It is shown that low mush permeability favors positive macrosegregations adjacent to the wall and strong negative segregations at the center line. In contrast, a higher permeability favors significant negative macrosegregations at the wall and at the center line and positive macrosegregations between wall and center line. It is demonstrated how the different flow phenomena contribute to this finding.

### 1 Introduction

The most economical way to produce the Sn-Bronze alloy is continuous casting, but the inhomogeneous distribution of the solute elements in the solidified strand, known as macrosegregation, is one of the critical problems in this process (Kudashov et al., 2005). As an example, a typical macrosegregation profile in the cross section of a Sn-Bronze billet is shown in Figure 1. Here, positive macrosegregations at the billet surface and negative segregations in the billet center are apparent. In

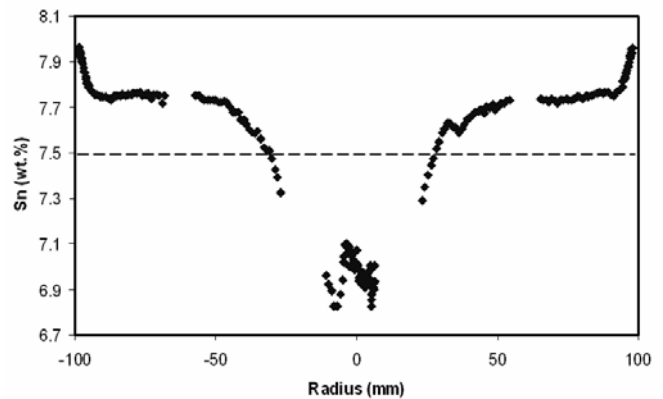


**Figure 1 :** Typical surface-to-surface Sn distribution in a Sn-Bronze cylindrical billet.

the last decades great efforts have been made to understand the formation of this kind of solute inhomogeneity during solidification. A general conclusion can be drawn (Lan et al., 2005, Amberg et al., 2005, Flemings, 2000, Ludwig et al., 2005, Beckermann, 2002): Macrosegregations are originated from mushy zone processes. They are caused by the relative motion between different phases with the mechanisms such as thermal-solutal convection, force convection, feeding flow due to solidification shrinkage, grain sedimentation, etc. Some modeling works were carried out in continuous (or direct chill) castings, but most of them are on Al alloys (Vreeman et al., 2000, 2000a, Reddy et al., 1997, Rousset et al., 1995). Moreover, due to the nature of the complexity of the multiphase phenomena, only partial success was achieved.

The idea to treat the mushy zone as separated phases, i.e. the solidified dendrite and the interdendritic melt, started in later 1980's (Voller et al., 1989, Rappaz et al., 1987, 1987a, 1990, Beckermann et al., 1993). It is generally assumed that ideal diffusion occurs in the interdendritic melt, and the volume averaged concentration of the interdendritic melt  $c_l$  is equal to the equilibrium concentration  $c_l^*$ . This approach was later extended (Beckermann

<sup>1</sup> Correspondence author, Email: ludwig@unileoben.ac.at

<sup>2</sup> Christian-Doppler-Laboratory for Multiphase Modeling of Metallurgical Processes, Department of Metallurgy, University of Leoben, Austria

<sup>3</sup> Wieland-Werke AG, Ulm, Germany

et al., 1993) to consider more general non-equilibrium situation, i.e.  $c_l \neq c_l^*$ . Very recently a 3-phase model for mixed columnar-equiaxed solidification was developed based on the previous globular-equiaxed solidification approach by two of the authors (Ludwig et al, 2005, 2002, Wu et al., 2003, 2003a, 2006). In this solidification model the morphologies of the columnar and equiaxed phases are simplified as cylinders and spheres correspondingly, but the competitive growth of both columnar and equiaxed phases, melt convection, equiaxed grain sedimentation, and their influence on the species transport and on macrosegregations, are taken into account.

This paper will focus on columnar solidification. The above mentioned 3-phase model is used, but the nucleation and growth of the equiaxed phase is ignored. The modeling work and results of the comprehensive case which includes both columnar and free-moving equiaxed grains in the Sn-Bronze continuous casting will be presented later. In the reduced, two-phase columnar solidification, the permeable mushy zone is assumed to be composed of cone-shaped 'dendrites' with a given primary dendrite arm spacing  $\lambda_1$ . Feeding flow, as well as thermal and solutal buoyancy flow, appear throughout the mushy zone. In a previous publication (Gruber-Pretzler et al., 2005) the results of four different case studies were reported, by separating the individual convection mechanisms: (i) considering only feeding flow; (ii) considering only thermal buoyancy flow; (iii) considering only solutal buoyancy flow; and (iv) considering only inlet jet flow by ignoring the feeding flow and thermo- solutal convection. In all of the 4 cases the same Blake-Kozeny-type mush permeability model was assumed. The modeling result of the case which combines all of the above convection mechanisms is presented here. Additionally, similar cases to those mentioned above will be repeated here, but this time with a higher Blake-Kozeny-type mush permeability. By comparing the case studies, a deeper understanding of the formation of macrosegregations in the Sn-Bronze continuous casting was achieved.

## 2 Model Description

The main assumptions of the model used can be summed up as follows:

- The thermodynamic for the binary CuSn system is approximated by using a constant redistribution coefficient,  $k$ , and a constant liquidus slope,  $m$ . The

solid fraction at the peritectic temperature reaches about 95-98%. Therefore, and because the model for the peritectic reaction is still under development, it is assumed that the remaining liquid solidifies over a small temperature interval.

- Nucleation and growth of equiaxed grains are ignored.
- Columnar dendrites are thought to start growing at the mold wall as soon as the temperature drops below the liquidus temperature.
- Growing cylinders are used to approximate the columnar dendrites.
- A shell-like growth driven by diffusion around the cylinder is assumed.
- Corresponding source terms to account for feeding flow and thermo-solutal buoyancy driven flow are included.
- Mechanical interaction between the mush and the flow is calculated via Darcy's law.
- To model the mush permeability the Blake-Kozeny permeability approach (Ludwig et al., 2002, Bird et al., 1960) is applied.

### 2.1 General Assumptions

1. Two phases are defined: the liquid phase ( $l$ ) as the primary and the columnar as the secondary phase ( $c$ ). The corresponding phase fractions are given as  $f_l$  and  $f_c$  with  $f_l + f_c = 1$ . The primary phase is thought to be a moving phase for which the corresponding Navier-Stokes equations is solved. The columnar phase is assumed to start growing from the mold wall, and to move with the constant and predefined pulling velocity  $\vec{u}_{cast}$ . Thus, no momentum conservation equation for the columnar phase is considered.
2. The columnar dendrites are assumed to have an ideal cone-shaped morphology (cellular dendrite-like).
3. A constant value for the primary arm spacing of columnar dendrites,  $\lambda_1$ , is assumed.

## 2.2 Mass Conservation and Growth Kinetics

The mass conservation equations for the liquid and the columnar phase are given as

$$\frac{\partial}{\partial t} (f_l \rho_l) + \nabla \cdot (f_l \rho_l \vec{u}_l) = M_{cl}, \quad (1)$$

$$\frac{\partial}{\partial t} (f_c \rho_c) + \nabla \cdot (f_c \rho_c \vec{u}_c) = M_{lc}. \quad (2)$$

Here,  $\rho_l, \rho_c$  are the densities and  $\vec{u}_l, \vec{u}_c$  the volume-averaged velocities of the different phases. The source term,  $M_{lc} (= -M_{cl})$ , represent the net mass transfer rate from the liquid to the columnar phase ( $\text{kg/m}^3/\text{s}$ ). For solidification it is positive and for melting negative.

In order to define the net mass transfer rate, the diffusion controlled growth kinetics around a piece-wise cylindrical dendrite trunk is modeled by considering the growth velocity in the radial direction

$$v_{R_c} = \frac{dR_c}{dt} = \frac{D_l}{R_c} \cdot \frac{c_l^* - c_l}{c_l^* - c_s^*} \ln^{-1} \left( \frac{R_f}{R_c} \right). \quad (3)$$

Here,  $c_l^*$  and  $c_s^*$  are the equilibrium liquid and solid concentrations adjacent to the solid/liquid interface, for which  $c_s^* = kc_l^*$  and  $c_l^* = (T - T_f)/m$ .  $D_l$  is the diffusion coefficient in the liquid.  $R_c = d_c/2$  is the average radius of a cylindrical dendrite trunk, and  $R_f = \lambda_1/2$  is half of the primary arm spacing,  $\lambda_1$ . With Eq. (3) we can define the volume-averaged net mass transfer rate by combining the total surface area of columnar dendrite trunks per volume  $S_A = \pi d_c / \lambda_1^2$ , and an Avrami-factor  $f_l$  to become

$$M_{lc} = v_{R_c} \cdot (\pi d_c / \lambda_1^2) \cdot \rho_c \cdot f_l \quad (4)$$

and with Eq. (3)

$$M_{lc} = \frac{D_l}{(d_c/2) \cdot (1-k)} \cdot \left( 1 - \frac{c_l}{(T - T_f)/m} \right) \cdot \ln^{-1} \left( \frac{\lambda_1}{d_c} \right) \cdot (\pi d_c / \lambda_1^2) \cdot \rho_c \cdot f_l. \quad (5)$$

This approach leads to a mass transfer as soon as the temperature dependent interface concentration in the liquid,  $c_l^* = (T - T_f)/m$ , exceeds the average liquid concentration,  $c_l$ , available in the corresponding volume element.

## 2.3 Momentum Conservation and Viscous Interaction Between Phases

The velocity field of the melt is obtained by solving the Navier-Stokes equation

$$\frac{\partial}{\partial t} (f_l \rho_l \vec{u}_l) + \nabla \cdot (f_l \rho_l \vec{u}_l \otimes \vec{u}_l) = -f_l \nabla p + \nabla \cdot \vec{\tau}_l + f_l \rho_l \vec{g} + \vec{U}_{cl}, \quad (6)$$

with  $\vec{\tau}_l = \mu_l f_l \left( \nabla \otimes \vec{u}_l + \left( \nabla \otimes \vec{u}_l \right)^T \right)$  being the stress-strain tensor of the liquid phase and  $\rho_l(T, c) = \rho_l^{ref} \cdot [1 + \beta_T \cdot (T^{ref} - T_l) + \beta_c \cdot (c^{ref} - c_l)]$  the temperature and concentration dependent density. The momentum exchange between the melt and the columnar dendrites consists of a contribution due to the phase transition,  $\vec{U}_{lc}^p$ , and a contribution due to the drag force between liquid and solid,  $\vec{U}_{lc}^d$ . Thus, we have  $\vec{U}_{lc} = \vec{U}_{lc}^p + \vec{U}_{lc}^d$ . The contribution due to phase change is described by  $\vec{U}_{lc}^p = \vec{u}^* \cdot M_{lc}$  with  $\vec{u}^* = \vec{u}_l$  for solidification and  $\vec{u}^* = \vec{u}_c$  for melting. The momentum exchange due to drag is modeled by using the Blake-Kozeny approach (Wu et al., 2005a). Thus, we used  $\vec{U}_{lc}^d = K_{lc} \cdot (\vec{u}_l - \vec{u}_c)$  with the drag coefficient given by  $K_{lc} = -f_l^2 \mu_l / K$  and a permeability taken as

$$K = K_0 \frac{f_l^3}{(1 - f_l)^2}, \quad (7)$$

with  $K_0 = \bar{K}_0 \cdot \lambda_1^2$ , where the pre-factor  $\bar{K}_0$  is assumed to be constant. Further details on the applied momentum exchange approach can be found in former publications by the authors (Ludwig et al., 2002, Wu et al., 2003, Wu et al., 2003a).

## 2.4 Species Conservation and Solute Partitioning at the Solid/Liquid Interface

The volume-averaged concentration  $c_l$  in the liquid, and  $c_c$  in the columnar phase are obtained by solving the species concentration equations

$$\frac{\partial}{\partial t} (f_l \rho_l c_l) + \nabla \cdot (f_l \rho_l \vec{u}_l c_l) = \nabla \cdot (f_l \rho_l D_l \nabla c_l) + C_{cl}, \quad (8)$$

$$\frac{\partial}{\partial t} (f_c \rho_c c_c) + \nabla \cdot (f_c \rho_c \vec{u}_c c_c) = \nabla \cdot (f_c \rho_c D_c \nabla c_c) + C_{lc}.$$

The solute exchange among liquid and solid is caused by solute partitioning at the solid/liquid interface. It is straight forward, that the corresponding exchange term is given by  $C_{lc}^p = c^* \cdot M_{lc}$ , where we assume  $c^* = k \cdot c_l^*$  for solidification and  $c^* = c_s^*$  for melting.

## 2.5 Enthalpy Conservation

We solve the enthalpy conservation equation for each phase

$$\frac{\partial}{\partial t} (f_l \rho_l h_l) + \nabla \cdot (f_l \rho_l \vec{u}_l h_l) = \nabla \cdot (f_l k_l \nabla \cdot T_l) + Q_{cl}, \quad (10)$$

$$\frac{\partial}{\partial t} (f_c \rho_c h_c) + \nabla \cdot (f_c \rho_c \vec{u}_c h_c) = \nabla \cdot (f_c k_c \nabla \cdot T_c) + Q_{lc}, \quad (11)$$

where the enthalpies are defined via  $h_l = \int_{T_{ref}}^{T_l} c_{p(l)} dT + h_l^{ref}$  and  $h_c = \int_{T_{ref}}^{T_c} c_{p(s)} dT + h_c^{ref}$  with the specific heat of the liquid being  $c_{p(l)}$  and that of the solid phase being  $c_{p(s)}$ .  $T_{ref}$ ,  $h_l^{ref}$  and  $h_c^{ref}$  are defined so that the enthalpy difference between the liquid and any solid,  $(h_l - h_c)$ , is equal to the latent heat of fusion. The release of latent heat and the enthalpy exchange between the phases are treated by  $Q_{lc}^p = h^* \cdot M_{lc}$ , where we assume  $h^* = h_l$  for solidification and  $h^* = h_s$  for melting. By solving the above conservation equations, Eq. (10)-(11), two different temperatures,  $T_l$  and  $T_c$ , were gained. In order to balance the temperatures between the two phases ( $T_l \approx T_c$ ), a quite large volume heat exchange coefficient of  $H^* = 10^8$  W/m<sup>3</sup>/K is used. Thus, we have a volume heat exchange of  $Q_{lc}^d = H^* \cdot (T_l - T_c)$ . It was verified in a previous publication (Rappaz et al., 1990) that the calculated temperature difference between liquid and solid in the mushy zone, where a large amount of latent heat is released, is about 0.2 K.

## 2.6 Auxiliary Quantities

In order to study the macrosegregation quantitatively, a mixture concentration,  $c_{mix}$ , is defined according to

$$c_{mix} = \frac{c_l \cdot \rho_l \cdot f_l + c_c \cdot \rho_c \cdot f_c}{\rho_l \cdot f_l + \rho_c \cdot f_c}. \quad (12)$$

(9) The volume averaging approach relates the volume fraction of the piece-wise cylindrical dendrites to the ratio of the average cross section area of a single trunk,  $\pi \cdot (d_c/2)^2$ , to the highest available area for a hexagonal<sup>4</sup> dendrite area

$$f_c = \frac{3}{4} \cdot \frac{d_c^2}{\lambda_1^2}. \quad (13)$$

This geometrical relation is used to determine the volume-averaged dendrite trunk diameter,  $d_c$ . Here,  $f_c$  is known from the corresponding mass conservation equation (Eq. (2)), and  $\lambda_1$  is given. For the results presented in Section IV we have used  $\lambda_1 = 144 \mu\text{m}$ .

## 2.7 Numerical Implementation

The conservation equations are numerically solved using the control-volume based finite difference CFD software FLUENT, version 6.2. FLUENT is a trademark of Fluent Inc. USA. All phases share a single pressure field,  $p$ . The pressure correction equation is obtained from the sum of the normalized mass continuity equations using a so-called Phase Coupled SIMPLE (PC-SIMPLE) algorithm (Fluent, 2003). For each time step 25 iterations are calculated to decrease the normalized residuals of  $c_l$ ,  $c_c$ ,  $f_c$ ,  $\vec{u}_l$  and  $p$  to a value below the convergence limit of  $10^{-4}$ , and  $h_l$  and  $h_c$  below that of  $10^{-7}$ . For each iteration the auxiliary quantity,  $d_c$ , is updated first. Then, based on the last iteration, the exchange terms  $U_{lc}$ ,  $C_{lc}$ ,  $Q_{lc}$  and  $M_{lc}$  are calculated. Finally, the 8 conservation equations<sup>5</sup> for the corresponding momentum, masses, enthalpies and species are solved simultaneously, which means coupled by the amount of the different phases and the exchange terms.

The FLUENT formulation is fully implicit, so there is no stability criterion that has to be met. However, due to the complexity of the present problem, the time step,  $\Delta t$ , should not be too large in order to meet convergence. The optimal time step must be determined empirically by test simulations. For the results presented in Section IV, a time step of  $\Delta t = 0.02\text{s}$  was used. In some cases it was adjusted to  $\Delta t = 0.002\text{s}$  at a later stage to increase numerical stability. Further discussion about calculation accuracy and the effect mesh quality (size) has upon it can be

<sup>4</sup>For a cubic area the pre-factor in Eq. (13) would be  $\pi/4$  instead of  $3/4$ .

<sup>5</sup>There are 8 equations in 2D (we count 2 equations for the momentum of melt) and 9 in 3D.

found in previous publications (Ludwig et al., 2002, Wu et al., 2003, 2003a).

### 3 Definition of the Benchmark Considered

#### 3.1 Geometry and Boundary Conditions

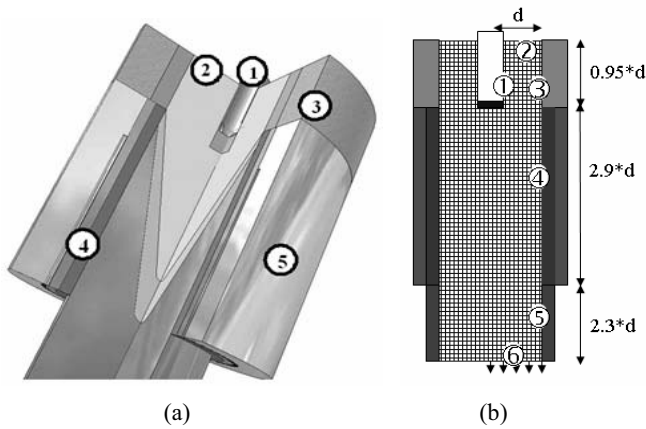


**Figure 2 :** (a) Sketch of the considered DC casting process: ① nozzle; ② free surface; ③ graphite mold with isolation; ④ graphite and copper mold; ⑤ steel mold with water cooling. (b) Grid and interfaces for boundary conditions (details given in the text).

For all presented calculations exactly the same geometry and boundary conditions as in (Gruber-Pretzler et al. 2005) and (Ludwig et al. 2005a) are used to allow an accurate comparison. For the process simulation a casting velocity of  $u_{ccast} = 1.92\text{mm/s}$  and a casting temperature of  $T_0 = 1389\text{ K}$  are used. Since the mold is of a cylindrical shape, an axis symmetrical simulation has been chosen. Fig. 2a is a schematic diagram showing the mold where (①) indicates the position of the nozzle, (②) shows the free surface on the top, (③) indicates the upper part of the mold which is assumed to be insulating, (④) shows the lower part of the graphite mold which is surrounded by a copper-steel mold including a water cooling system (⑤). Fig. 2b gives an overview over the boundary conditions used. Here (①) gives the position of the inlet, where a pressure inlet is taken. A heat transfer coefficient (HTC) of  $h = 50\text{ W/m}^2\text{K}$  and a nozzle temperature of  $T_{SEN} = 1292\text{ K}$  are considered for the submerged entry nozzle (SEN) region. For (①) the HTC and the temperature have a value of  $h = 50\text{ W/m}^2\text{K}$  and  $T_{surface} = 325\text{ K}$ . For (②) almost ideal insulation is assumed with  $h = 10\text{ W/m}^2\text{K}$  and  $T_{mold} = 1292\text{ K}$ . For

(③)  $h = 3000\text{ W/m}^2\text{K}$  and  $T_{mold} = 550\text{ K}$  and for (④)  $h = 1000\text{ W/m}^2\text{K}$  and  $T_{water} = 300\text{ K}$ . The constant velocity  $u_{cast} = 1.92\text{mm/s}$  is taken for the outlet (⑤). For the nozzle and for the free surface a slip condition is used. The mold wall is assumed to move with casting velocity. Therefore, a slip condition for the liquid phase and a non-slip condition for the columnar phase are applied. The grid used has a size of 9016 cells and 9296 nodes. As initial conditions, we started with hot melt ( $T_{init} = 1292\text{ K}$ ) at rest ( $u_{cast} = 0\text{m/s}$ ). The presented results are taken after reaching a steady state.

#### 3.2 Case Description

In order to estimate the relative importance of feeding flow, thermal and solutal buoyancy flow, and inlet flow depending on mush permeability, the simulation results of 10 different cases are discussed.

Two different values for the empirical factor in the Blake-Kozeny expression (Eq. (7)) are considered, namely i)  $\bar{K}_0 = 1.4 \cdot 10^{-3}$  and ii)  $\bar{K}_0 = 1.4 \cdot 10^{-5}$ . In addition to the 4 cases studied in Wu et al. (2003), one simulation for each  $K_0$  covering all 4 phenomena is performed. The 5 cases, discussed for both mush permeabilities, can be described as following:

- Case A: No thermal and solutal buoyancy flow and no feeding flow are considered. We used equal densities for the liquid and the solid.
- Case B: Here only solutal buoyancy flow is considered. The solutal expansion coefficient was chosen to be  $\beta_c = 0.11\text{ wt.\%}^{-1}$  (calculated after (Miettinen, 2005)).
- Case C: Here only thermal buoyancy flow is considered. The thermal expansion coefficient was chosen to be  $\beta_T = 8.6 \cdot 10^{-5}\text{ K}^{-1}$  (calculated after (Miettinen, 2005)).
- Case D: For this simulation only feeding flow is considered. So we assumed the liquid and solid densities to be independent of temperature and concentration, but different. During solidification the higher solid density then leads to a shrinkage-induced feeding flow.
- Case E: This simulation includes thermal and solutal buoyancy flow in addition to feeding induced flow and forced convection.

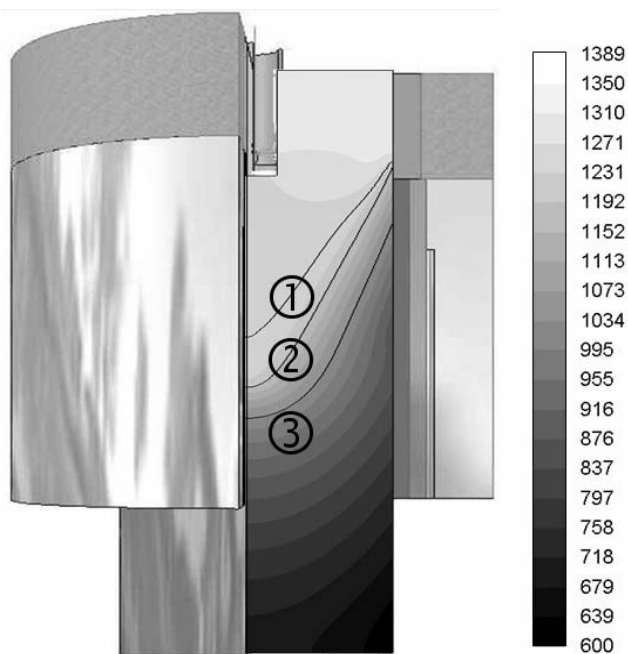


**Figure 3** : Temperature field of the casting (scaled in K) in the case where just inlet flow is considered (Case A-L). ①  $T_{liquid}=1289$  K; ②  $T_{solidus} = 1230$  K; ③  $T_E=1072$  K.

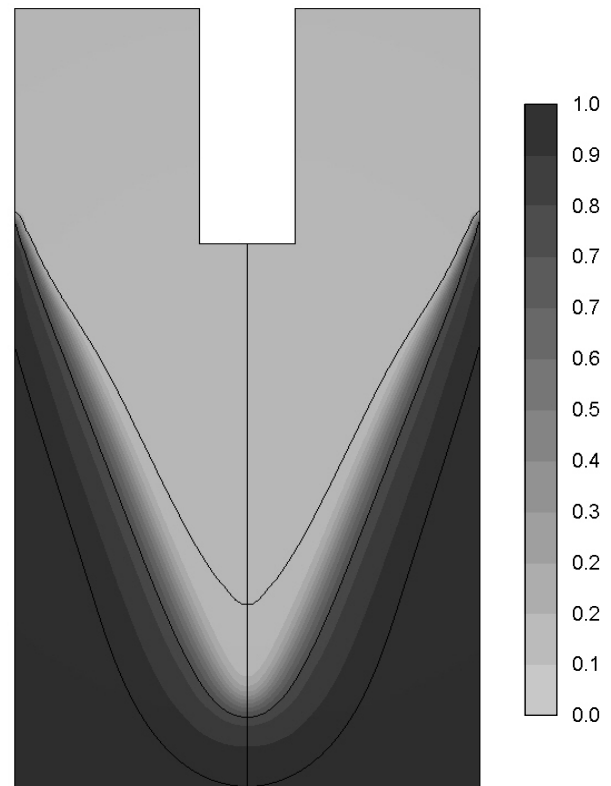


**Figure 4** : Volume fraction of the columnar phase (scaled in %) in the case where just inlet flow is considered (Case A-L). Black lines show the isotherms corresponding to the same values as mentioned in Fig 2.

To distinguish between low and high permeability calculations, the different cases are labeled with L for low permeability or H for high permeability.

## 4 Results And Discussion

### 4.1 General Solidification Sequences

The studied continuous casting process of a CuSn6 alloy starts with the melt preheated to the casting temperature of  $T_0 = 1389$  K. The hot melt enters the mold through one nozzle in the center of the casting. Due to the fact that the upper part of the mold is thought to be insulating, cooling starts where the hot melt reaches the water cooled graphite mold. Fig. 3 shows the calculated steady state temperature field of Case A-L. Solidification starts at the liquidus temperature of CuSn6, namely at  $T_{liquid}=1289$  K (①, Fig. 3) and is completed at the end temperature of  $T_E=1072$  K (③, Fig. 3). This temperature represents the peritectic temperature of the binary CuSn sys-

tem. Based on the fact that the casting reaches a solid fraction of about 95% at  $T_E$ , and because the model for the peritectic reactions is still under development, it is assumed that the remaining liquid solidifies over a small temperature interval at  $T_E$ . The third black line between the aforementioned two lines shows the isotherm of the solidus temperature of CuSn6,  $T_{solidus} = 1230$  K (②, Fig. 3). Fig. 4 shows the volume fraction of the columnar phase in Case A-L. It can be seen that in the columnar mushy zone, extending from  $T_L$  to  $T_E$ , the volume fraction of the solid varies from 0 to 1.

As we considered the mush to be permeable, melt-flow occurs through the mush. Fig. 5 shows the velocity magnitude of the continuous casting process simulated in Case A-L. It can easily be seen that the flow velocities in the mush are much smaller compared to the inlet flow velocities. The incoming melt reveals a velocity as high as  $u_{in} = 25$  mm/s. This large value is a consequence of the constant outlet velocity,  $u_{cast}$ , and the overall mass cons-

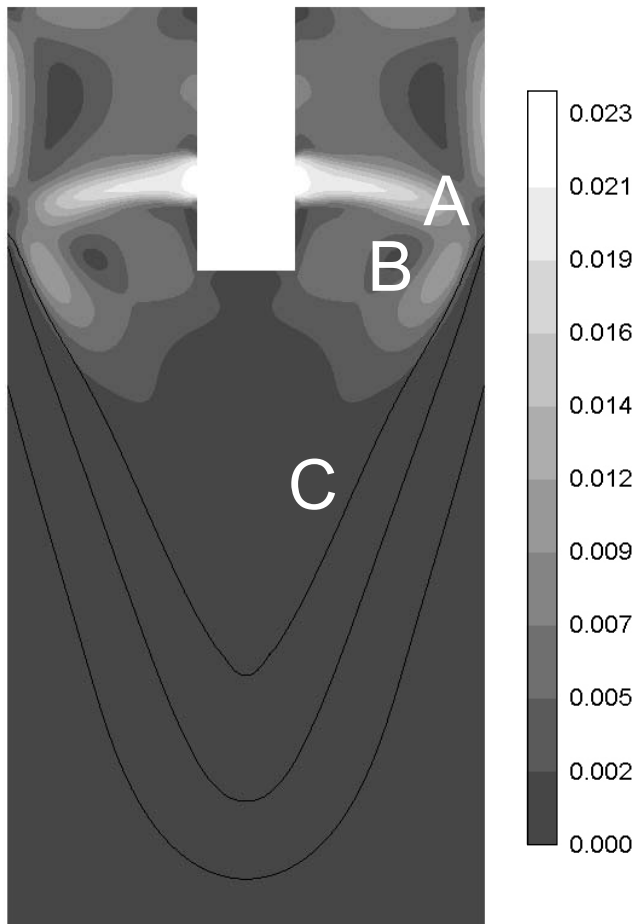


**Figure 5** : Velocity field of the casting (scaled in m/s) in Case A-L where just inlet flow is considered. A: Inlet bending at the wall; B: vortex; C: casting velocity is reached.

servation. The developing flow pattern shows a strong inlet jet that reaches the wall almost horizontally (A, Fig. 5). Then the jet bends inwards towards the center while slowing down and creating one large vortex on each side of the casting (B, Fig. 5). The velocity of the liquid flow is decreased because of interaction with the solidifying dendrites in the mushy zone. After achieving a certain solid content, the liquid is forced to move with the same velocity as the solid phase due to the drag force acting between the liquid and the columnar phase (C, Fig. 5). In addition, the influence of the jet diminishes at a certain depth in the center of the casting. Although the velocity regime does not create turbulent flow ( $Re \approx 900$ ), the developing jet plays an important role for the solute depletion and accumulation during solidification.

Due to microsegregation the tin concentration in the liquid between the dendrites changes during the solidification process. Since the solute is enriched in the liquid phase, the intensity of the flow field has a huge impact on the alloy distribution in the solidified casting. In general three cases have to be mentioned (Flemings et al., 1967, 1967a):

No relative fluid flow occurs in the interdendritic region. In this case the mixed concentration of the solidified casting is the same as the original alloy concentration.

The relative velocity of the liquid in the interdendritic region is higher than the casting velocity, and the growing solid is fed by non segregated fresh melt. This situation causes negative macroseggregations.

The growing dendrites are fed with already segregated melt: Here positive macrosegregation occurs, so called inverse macrosegregation.

#### 4.2 Jet-Mush Interaction

The simulation of the casting process where only forced convection is taken into account shows the influence of the relatively high velocities of the inlet jets on the temperature distribution, the velocity field and the macrosegregation.

As mentioned earlier, the inlet jets hit the mold close to the region where the first solid is formed, bend inwards and form corresponding vortices. Fig. 6 shows the temperature field achieved in Case A-L (Fig. 6a) and Case A-H (Fig. 6b), whereas Fig. 7 states the velocity fields of both cases. The differences in the position of the isotherms of  $T_{liquid}=1289\text{ K}$  ((①), Fig. 6) and  $T_E=1072\text{ K}$  ((②), Fig. 6) are a direct result of the change in the velocity field, due to the change in mush permeability. Note that with a higher mush permeability (Case H), the vortices caused by the inlet jet are slightly wider and to some extent larger. As a consequence the liquidus isotherm is shifted upwards in the center of the casting. The isotherm representing the end of solidification stays at almost the same level. Fig. 7 shows that the inlet region is the only part of the casting that has a velocity magnitude as high as  $u \approx 3 \cdot 10^{-2}\text{ m/s}$ . As soon as the mushy zone is reached, the jet slows down and the velocity of the liquid is, due to the applied drag force between the columnar phase and the liquid phase, governed more and more by the casting speed ((①), Fig. 7). Because of the chosen  $\bar{K}_0$ , the vortices of the inlet jets

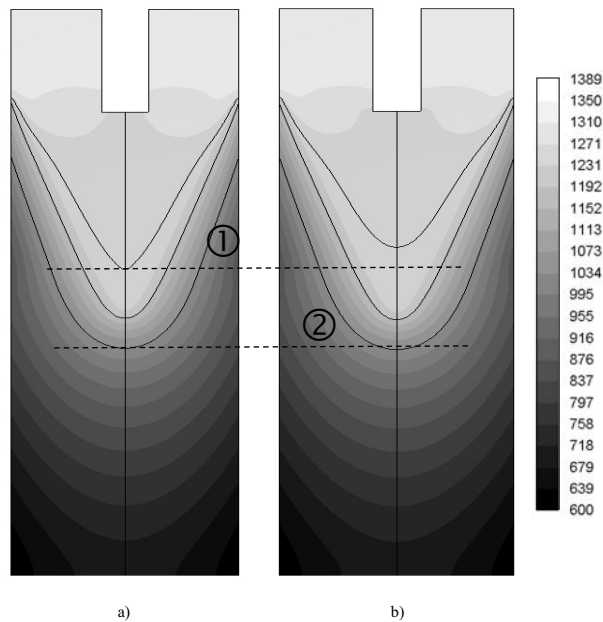


**Figure 6 :** Temperature field of the casting (scaled in K) in (a) Case A-L and (b) Case A-H where just inlet flow is considered. As guidance, the dotted lines show ① position of  $T_{liquid}=1289$  K and ② position of  $T_E=1072$  K at the center of the casting in Case A-L.

penetrate into the mushy zone differently for the L and H cases. In Case A-H, the high permeability of the mush allows the liquid to somehow reach deeper into the mush (②), Fig. 7). Therefore, segregated melt is removed from the mushy zone and replaced by non-segregated, ‘fresh’ melt from the jet vortices. This ‘jet-mush’ interaction phenomenon takes more intensively place in all cases considered (labeled with I in Fig. 16, Fig. 17). Its strength depends on the velocity of the jet on the one hand and on the permeability of the mush on the other. The higher the mush permeability, the more intensely the jet can meet the mushy zone and wash out an increasing amount of segregated melt. This then results in strong negative surface macrosegregations and more significant positive ‘bulk’ macrosegregations (Fig. 16, Fig. 17).

### 4.3 Solutal Buoyancy

In addition to the inlet jet, solutal buoyancy convection is taken into account in Case B-L and B-H (labeled with IIa in Fig. 9b, Fig. 17b). The solutal buoyancy driven flow shows no significant influence at the temperature field in

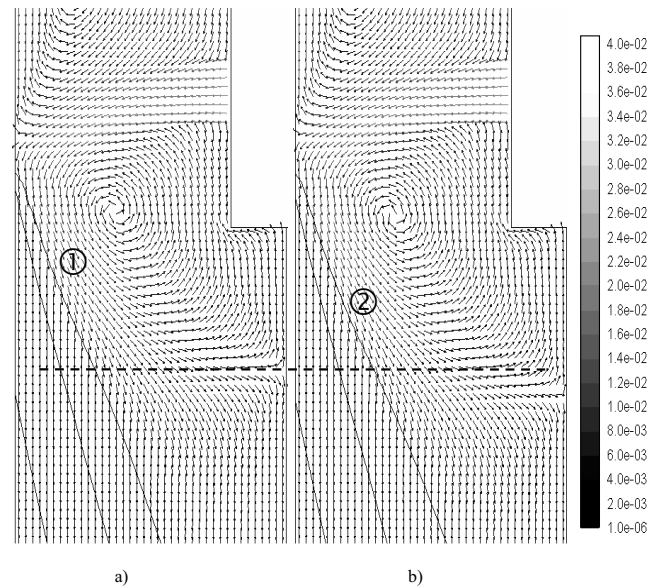


**Figure 7 :** Velocity field of the upper part of the casting (scaled in m/s) in (a) Case A-L and (b) Case A-H where just inlet flow is considered. Note that with a higher mush permeability (Case H), the vortices caused by the inlet jet, are slightly wider and to some extent larger. As a consequence the liquidus isotherm is shifted upwards in the center of the casting. The isotherm representing the end of solidification stays at almost the same level.

Case B-L (Fig. 8a). But, increasing the mush permeability offers more freedom to the flow and therefore changes the temperature distribution in Case B-H, which results in a slightly lower isoline for  $T_{liquid}=1289$  K (①, Fig. 8b) in comparison to Case B-L, whereas  $T_E=1072$  K (②), Fig. 8b) stays at almost the same level. During solidification the liquid in the mushy zone becomes enriched in solute and thus tends to rise upwards through the mush by solutal buoyancy (labeled with IIa in Fig. 9b). In Case B-L the liquid is not able to move easily between the solidifying dendrites because the low permeability decreases the possibility of convection (Fig. 9a). So in this case an upward motion is not observed and therefore the macrosegregation pattern is not significantly different from that of Case A-L: the jet causes negative segregations right at the wall (Fig. 16a) and a slightly positive segregation occurs in the bulk of the casting (which can hardly be seen in Fig 16, due to the applied grey scale.). In Case B-H the high mush permeability allows solutal buoyancy flow to occur and therefore the macrosegregation pattern is influenced by it (labeled with IIa in Fig.

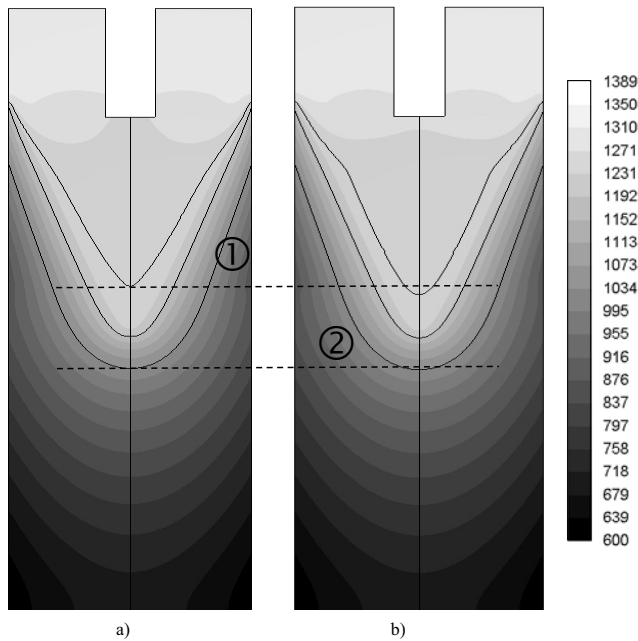


**Figure 8** : Temperature field of the casting (scaled in K) in (a) Case B-L and (b) Case B-H where inlet flow and solutal convection are considered. As guidance, the dotted lines show ① the position of  $T_{liquid}=1289$  K and ② the position of  $T_E=1072$  K at the center of the casting in Case B-L.

17b).

#### 4.4 Thermal Buoyancy

In addition to the inlet jet, thermal buoyancy convection is taken into account in Case C-L and C-H. This additional flow phenomenon changes the temperature field in the casting noticeably (Fig. 10a, b). The reason for this is the fact that thermal buoyancy flow strengthens the inlet jet vortex where the cooled melt flows down along the solidification front (labeled with II in Fig. 11a, b). The thermal buoyancy driven downward flow induces an upward flow in the center of the casting. Thus, melt is carried from deep down the melt pool upwards (labeled with III in Fig. 11a, b) and so the liquidus isotherm  $T_{liquid}=1289$  K (①), Fig. 10b) is shifted up in comparison to the first two discussed cases, whereas  $T_E=1072$  K (②), Fig. 10b) stays at about the same position as in Case A-L. This enlarges the mushy zone in comparison to Case A. As a consequence the ‘jet-mush’ interaction is increased and more segregated melt is washed out, which in turn leads to more extensive negative surface macrosegregations compared to Case A (Fig. 16a, c, Fig. 17a, c). The

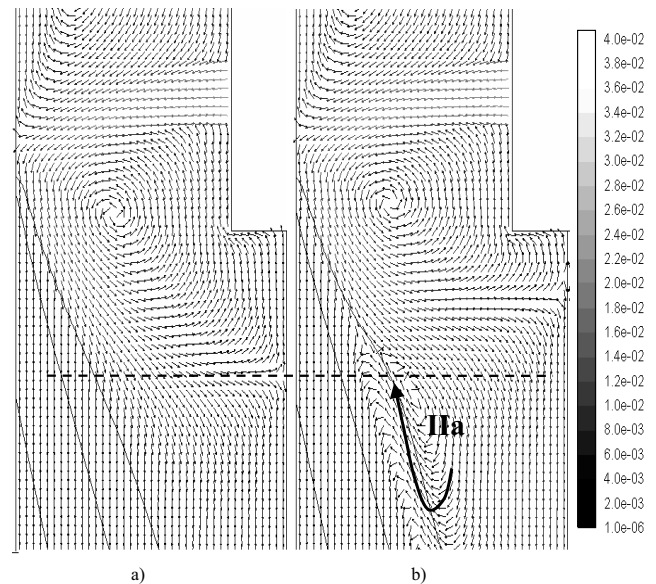


**Figure 9** : Velocity field of the upper part of the casting (scaled in m/s) in (a) Case B-L and (b) Case B-H where inlet flow and solutal convection are considered. IIa marks the upward rising liquid due to solutal buoyancy flow.

washed-out segregated melt is then accumulated in the middle of the casting, which is the reason for the positive macrosegregations in the ‘bulk’ of the strand. All these effects of the velocity field are strengthened in Case C-H. Fig. 11 shows the velocity fields of the upper part of the calculation domain of Case C-L (Fig. 11a) and C-H (Fig. 11b) including the “depth of penetration”, indicated by broken black lines. The “depth of penetration” empirically defines the border between areas, where the velocity of the liquid is significantly different from that of the solid phase and those where, both phases move with almost the same speed and direction; that’s where the drag caused by the columnar dendrites dominates. The “depth of penetration” corresponds to about 50% of the solid fraction in Case C-H and 20% in Case C-L. Due to a large “flow-through” mush area, the distribution of the macrosegregations is much more pronounced in Case C-H. In the cases considered so far macrosegregations are frozen below the “depth of penetration” (broken black line in Fig. 16c, Fig. 17c).

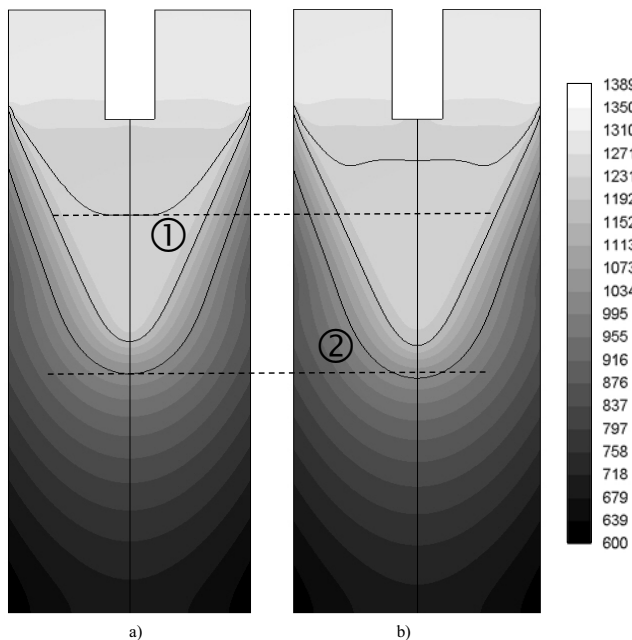


**Figure 10** : Temperature field of the casting (scaled in K) (a) in the case with thermal buoyancy flow (Case C-L), (b) the same case with a higher permeability (Case C-H). As guidance, the dotted lines show ① the position of  $T_{liquid}=1289$  K and ② the position of  $T_E=1072$  K at the center of the casting in Case C-L.

#### 4.5 Feeding Flow

Including feeding flow in Case D-L and D-H (Fig. 12 and 13) in addition to the forced convection of the inlet flow, the flow pattern changes in that a second higher velocity field appears in the mushy zone, right in the middle of the casting. This also induces a significant change in the temperature fields of both cases shown in Fig. 13a, b. The isotherms are moved downwards (Fig. 12) compared to Case A-L due to the fact that more liquid is needed to feed the solidification shrinkage. In Case D-H the high mush permeability causes a broadening of the mushy zone, which is shown by an upward movement of the  $T_{liquid}$  (① Fig. 12).

Up until now, surface macrosegregations are predicted to be negative and macrosegregations within the casting are predicted to be either negative or positive. However, if shrinkage-induced feeding flow is included and thermo-solutal buoyancy driven flow is ignored, the situation changes. In Case D-L the surface macrosegregations turned out to be positive and the macrosegregations in the center negative (Fig. 17d, see (Gruber-Pretzler et

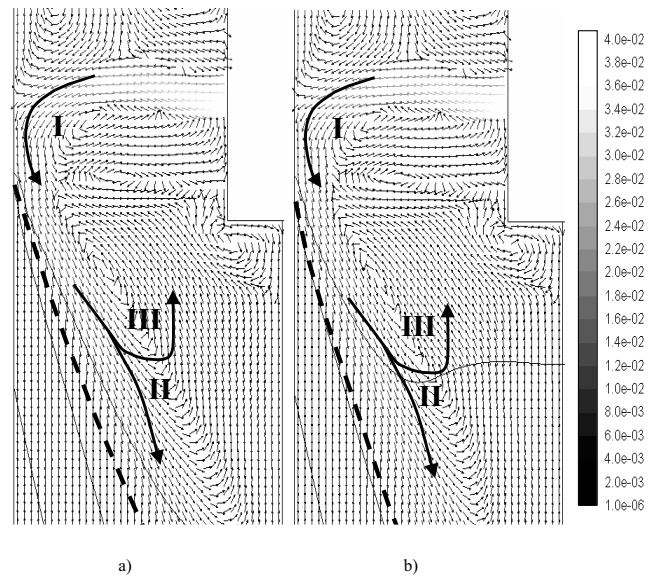


**Figure 11** : Velocity field at the inlet region (scaled in m/s) (a) in the case with thermal buoyancy flow (Case C-L), (b) the same case with a higher permeability (Case C-H). Broken black lines indicate the “depth of penetration” (see text).

al, 2005)), so just the opposite! Feeding flow is always directed from the dendrite tip towards its roots and thus carries segregated melt into the mush. Since the early work of Flemings in 1967 (Flemings et al., 1967, 1967a), this phenomenon is known to produce positive macrosegregation at the surface of a casting, the so-called inverse segregation<sup>6</sup>. Exactly this happens in Case D-L (labeled with IV in Fig. 16d). However, in Case D-H the influence of the jet is so high that negative macrosegregations still occur at the wall and the positive ones are moved to adjacent zones (labeled with IV in Fig. 17d). At the center of the cylindrical casting the dendrite tips approach each other and so form a ring which will close as the solidification proceeds. Besides, a relatively large mush area at the center is solidifying and thus a huge amount of melt is needed to feed the corresponding shrinkage. This feeding flow causes the melt to be sucked into the solidifying mush through the closing ‘ring of dendrites’ and

<sup>6</sup> Nowadays, inverse (surface) macrosegregation is also known to be caused by an interdendritic flow towards the surface, accompanied by reheating and remelting during the local formation of a gap between the casting and the mold.

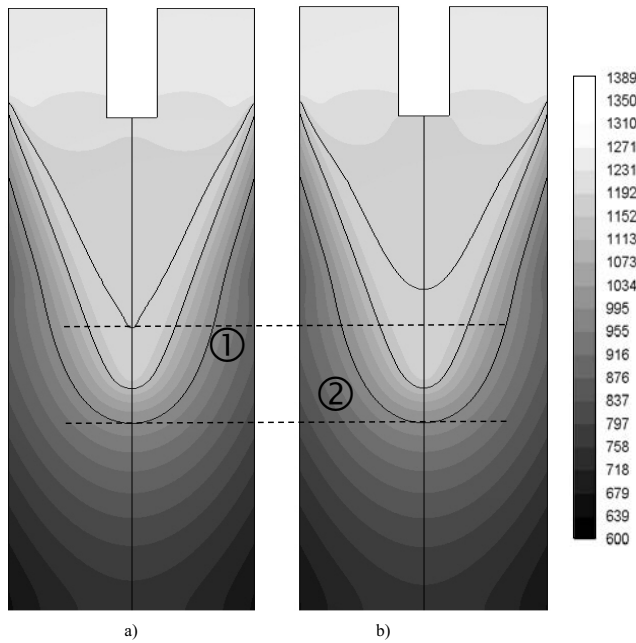


**Figure 12** : Temperature field of the casting (scaled in K) (a) in the case with feeding flow (Case D-L), (b) the same case with a higher permeability (Case D-H). As guidance, the dotted lines show ① the position of  $T_{liquid}=1289$  K and ② the position of  $T_E=1072$  K at the center of the casting in Case D-L.

a strong relative downward velocity occurs in the center of the casting (labeled with V in Fig. 16d, see ref. (Gruber-Pretzler et al., 2005), (Ludwig et al., 2005a)). That is why the solidifying dendrites are fed with less- or non-segregated ‘fresh’ melt from the melt pool and negative macroseggregations occur in the central region of the casting. In addition, heat is carried downwards with the feeding flow which results in a lower position of the isotherms, especially at the casting center. In Case D-L this phenomenon is more pronounced due to the low permeability compared to Case D-H. In the latter case, the large  $\bar{K}_0$  makes feeding through the mush easier. Therefore, the central downward flow is significantly broader and slower, which broadens and decreases the negative center line segregation (labeled with V in Fig. 17d).

#### 4.6 Relative Importance of the Different Phenomena

So far, the presented cases give separate sets of information about the influence each considered convection phenomenon has on the solidification process. For simulations including thermo-solutal buoyancy and feeding flow in addition to the forced convection of the inlet jet,

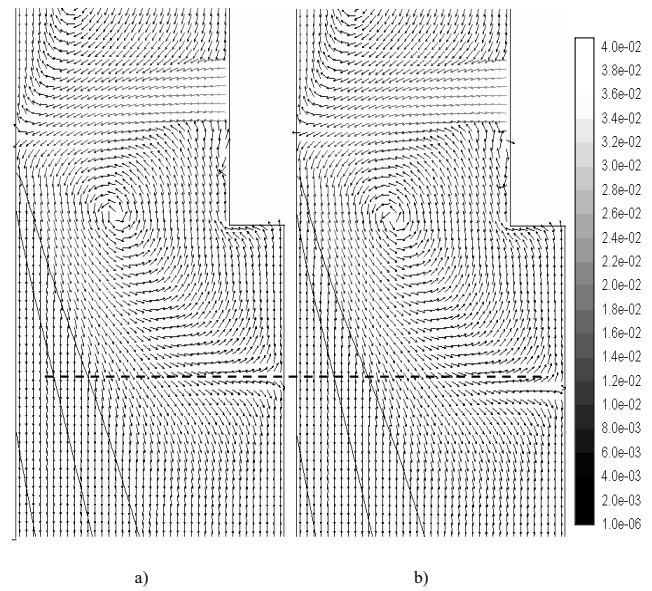


**Figure 13** : Velocity field at the inlet region (scaled in m/s) (a) in the case with feeding flow (Case D-L), (b) the same case with a higher permeability (Case D-H).

superposition of the different phenomena is expected, which indeed can be seen in Case E-L and Case E-H (Fig. 14, Fig. 15). The isolines in Case E-L (Fig. 14a) reflect a strong influence of both thermal convection and feeding flow. Hence, the melt pool is broadened and the liquid has more freedom to move, which can be seen by looking at the flow field in Fig. 15a. In Case E-H (Fig. 14b) all four studied flow phenomena are strengthened due to the higher permeability. In this case the solutal buoyancy driven flow plays an additional role in the solidification sequence. However, an upward flow caused by solutal buoyancy within the mush can not be observed in the combined case. It seems that the opposite downward thermal buoyancy has overwhelmed the upward solutal buoyancy. This can also be seen by the liquidus isotherm of Case E-H (Fig. 14) being shifted upwards, but not as much as in the purely thermal case, Case B-H (compare Fig. 9).

It is obvious that this change in the flow pattern has a huge effect on the solute distribution in the solidified casting. In Case E-L positive surface macroseggregations are predicted (Fig. 16e). Here, the impact of the feeding

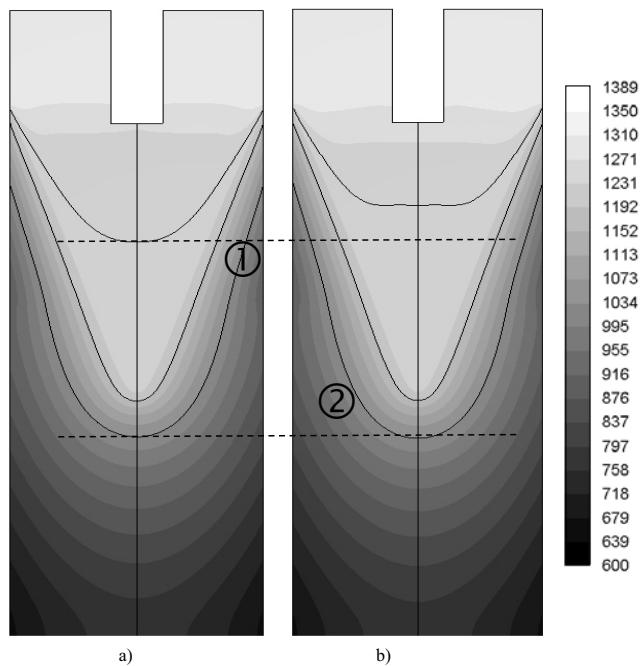


**Figure 14** : Temperature field of the casting (scaled in K) (a) in the combined case which considers inlet jet, solutal and thermal buoyancy, and feeding flow (Case E-L), (b) the same case with a higher permeability (Case E-H). As guidance, the dotted lines show ① the position of  $T_{liquid}=1289$  K and ② the position of  $T_E=1072$  K at the center of the casting in Case E-L.

flow on its formation is decreased by the inlet jet and the thermal buoyancy flow. Right at the center line strong negative macrosegregations appear, which are caused by the feeding flow but smoothed by the additional effect of thermal convection. In Case E-H the influence of the jet is so high that the negative surface macrosegregation is not overwhelmed by the effect of feeding flow. Therefore, in this case the macrosegregation pattern results in negative surface and centerline segregations and positive ones in the bulk of the casting (see next chapter).

#### 4.7 Impact of Mush Permeability on the Formation of Macroseggregations

In the implemented case two different values of  $\bar{K}_0$  have been considered for the calculation of the Blake-Kozeny-type mush permeability. Since no values for Copper alloys are available, those values are approximated from measurements on Aluminum alloys (Apelian et al., 1974). Fig. 16 and 17 show the computed macrosegregation patterns of the studied cases for a mush permeabil-

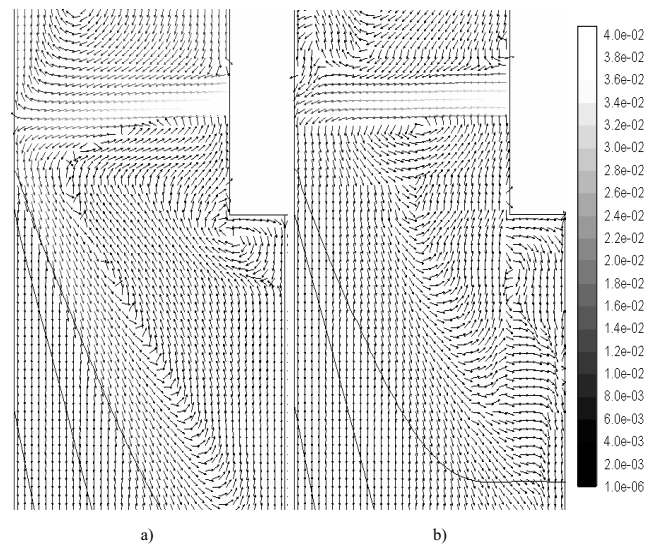


**Figure 15** : Velocity field at the inlet region (scaled in m/s) (a) in the combined case which considers inlet jet, solutal and thermal buoyancy, and feeding (Case E-L), (b) the same case with a higher permeability (Case E-H).

ity assumed to be characterized by  $\bar{K}_0 = 1.4 \cdot 10^{-3}$  and  $\bar{K}_0 = 1.4 \cdot 10^{-5}$ . By comparing these two figures it can be seen that, in general, an increase of  $\bar{K}_0$  leads to more pronounced macrosegregations.

In Case A-L and A-H the ‘jet-mush’ interaction phenomenon described above is not overlaid by other phenomena (labeled with I in Fig. 16a, Fig. 17a). The flow from the jet and the flow caused by the withdrawal of the strand are the only convection mechanisms present. However, even in these two cases the negative surface macrosegregations and the slightly positive ‘bulk’ macrosegregations can be observed. The comparison only shows very small positive segregations in Case A-L, but more significant ones in Case A-H.

Solutal buoyancy does not affect the macrosegregation pattern in the case of low a  $\bar{K}_0$  (Fig. 16b). In Case B-H the high mush permeability enables the enriched liquid to move upwards through the mush till it impinges on the jet flow (labeled with IIa in Fig. 17b). This causes positive macrosegregations at the corresponding position. On the

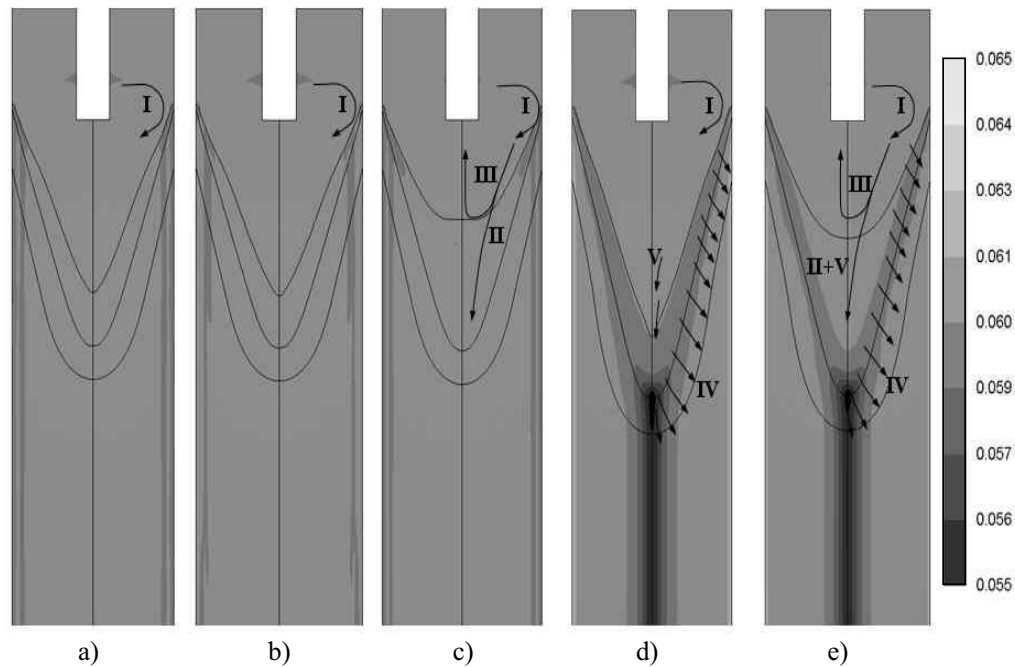


**Figure 16** : Steady-state distributions of the mixture concentration in the five different cases with a lower Blake-Kozeny-type mush permeability ( $\bar{K}_0 = 1.4 \cdot 10^{-3}$ ): (a) without feeding and thermo-solutal buoyancy flow (Case A-L); (b) only solutal buoyancy flow (Case B-L); (c) only thermal buoyancy flow (Case C-L) and (d) only feeding flow (Case D-L); (e) including feeding and thermo-solutal buoyancy flow (Case E-L). Bright green(Grey) represents the initial alloy concentration, yellow (white) represents positive and blue (black) negative macrosegregations. Flow patterns are indicated by arrows.

other hand, the solutal buoyancy driven flow out of the middle of the strand causes negative center line segregations.

When considering thermal buoyancy flow in Case C-L and C-H, the ‘jet-mush’ interaction is strengthened. This stronger flow pattern leads to more extensive negative surface macrosegregations compared to Case A. The washed-out segregated melt from the surface areas is accumulated by the flow in the middle of the casting. Thus, positive macrosegregations in the ‘bulk’ of the strand are predicted (labeled with II in Fig. 16c and Fig. 17c). The thermal buoyancy driven downward flow induces an upward flow in the center of the casting. With a larger mush permeability, this even leads to an upward transportation of washed-out alloy elements.

Besides, in Case C-H (Fig. 17c) the high mush permeability leads to significantly stronger macrosegregations for both negative ones at the wall and positive ones in the casting’s center.

The simulation of Case D-L (labeled with IV in Fig.

16d) predicts positive macrosegregations, namely inverse macrosegregations, at the wall, and negative ones in the center of the casting. This is described in more detail in Section 4.5. In Cases A, B, and C, the increase of the mush permeability was the reason for the strengthening of the forming macrosegregations. However, in Case D the increased mush permeability causes a total change in the macrosegregation pattern! On the one hand the influence of the jet is so high that negative macrosegregations occur at the wall and the positive ones are moved to adjacent zones, but on the other hand, the higher permeability makes feeding through the mush easier, and therefore the area between the solidifying dendrites in the center of the casting is not as small in Case D-H as in Case D-L. This leads to less pronounced but broadened negative macrosegregations in the center line.

In Case E all four flow phenomena are included. This leads to the prediction of positive macrosegregations at the surface and negative ones at the center line in Case E-L. Here, the impact of feeding flow on the formation

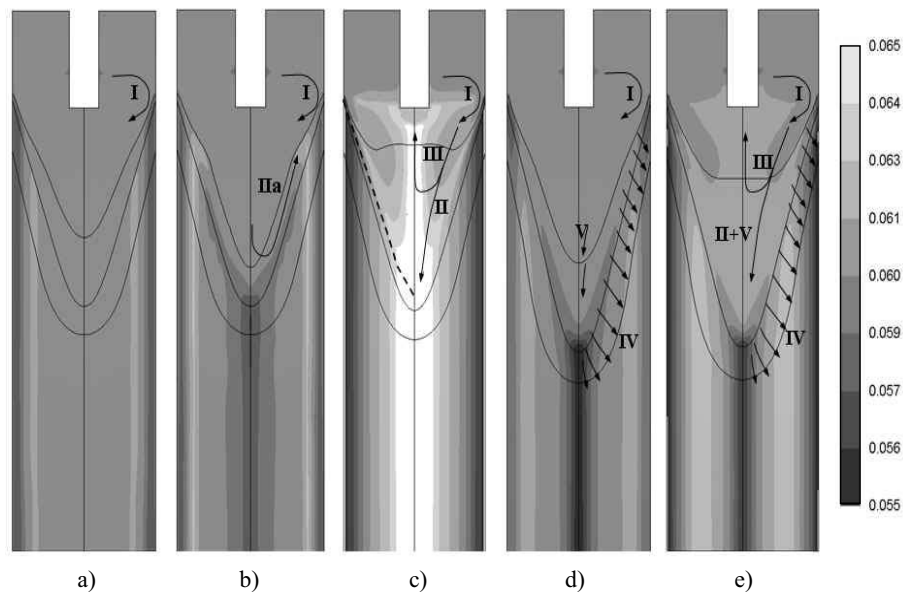


**Figure 17** : Steady-state distributions of the mixture concentration in the five cases with a higher Blake-Kozeny-type mush permeability ( $\bar{K}_0 = 1.4 \cdot 10^{-5}$ ): (a) without feeding and thermo-solutal buoyancy flow (Case A-H); (b) only solutal buoyancy flow (Case B-H); (c) only thermal buoyancy flow (Case C-H) and (d) only feeding flow (Case D-H); (e) including feeding and thermo-solutal buoyancy flow (Case E-H). Grey represents the initial alloy concentration, white represents positive and black negative macrosegregations. Flow patterns are indicated by arrows.

of macrosegregation is decreased by the inlet jet and the thermal buoyancy flow. Case E-H shows three significant differences compared to Case E-L. Firstly, the influence of the inlet jet is so large that negative surface segregations can be observed. Secondly, the positive macrosegregations in the bulk are stronger and broader compared to Case E-L. This is caused by a strengthening of the macrosegregations due to thermo-solutal buoyancy flow. Thirdly, the negative center line macrosegregations are not as pronounced as in Case E-L. In the center line of Case E-H, the strong positive macrosegregations caused by thermal convection (Fig. 17c) are overwhelmed by feeding flow (Fig. 17b, d).

The model based on current assumptions provides a numerical tool for qualitative study of macrosegregations. By comparing the simulation result (Figure 16e) with the experimental measurement (Figure 1), we do obtain a good qualitative agreement. However, in order to predict the macrosegregations quantitatively further refinements/improvements to the current model are necessary. Furthermore, some parameters used for the simulation must also be justified. Some important points are discussed as follows.

As studied in this paper, permeability is one of the most

important parameter influencing the macrosegregation in the continuous casting. Great efforts were made in last decades on this topic (Apelian et al., 1974, Schneider et al., 1995, Nielsen et al., 1999, Bernard et al., 2005, Goyeau et al., 1999). Further surveys and studies are required to get suitable model, for the permeability, especially when a special alloy is concerned.

It is of evidence that equiaxed solidification and grain sedimentation plays very important role in the formation of negative center segregations (Figure 1). The presented 2-phase model ignores nucleation, growth and sedimentation of equiaxed crystal. With the more advanced model for mixed columnar-equiaxed solidification recently suggested by two of the authors (Wu et al., 2006) these simplifications will be overcome in near future.

The current model is based on the assumption of simplified morphology: a shell-type growth driven by diffusion around cone-shaped 'dendrites'. In the mushy zone, the local average concentration of the interdendritic liquid,  $c_l$ , is supposed to be different from the local average equilibrium concentration at the solid/liquid interface,  $c_l^*$ . This difference is taken as the driving force for Regrowth of the columnar phase. In a previous publication by Wu

and Ludwig (Wu et al., 2006), detailed parameter studies on the  $c_l$  and  $c_l^*$  in the mushy zone were made. In a 1D unidirectional solidification, the species in the mushy zone is predicted to be gradually enriched with the evolution of the solid phase. Although  $c_l$  is predicted to be somehow smaller than  $c_l^*$ , especially in the region near to the columnar tips, the predicted  $c_l - f_c$  curve is quite close to the  $c_l^* - f_c$  curve according to the Scheil assumption (ideal diffusion in mushy zone). We also made a simulation with an artificially increased  $D_l$  and found that both the simulated  $c_l - f_c$  curve and the Scheil  $c_l^* - f_c$  curve are almost identical. It indicates that although a shell-type growth driven by diffusion around the cylinder is assumed, it reproduce closely the classical Scheil type mushy zone behavior.

As for the considered case the typical Reynolds-number is not larger than  $Re \approx 100$ , the simulation results presented in this paper did not include any turbulence flow. The highest Reynolds-numbers are found in the upper part of the pool region near the entry nozzle. Inside the pool and especially in the mushy zone the Reynolds-numbers are smaller by orders of magnitudes.

The numerical predictions depend strongly on the considered geometry and other casting properties. Therefore, any changes in casting conditions can influence the macrosegregation results significantly.

## 5 Conclusions

Macrosegregations in continuous casting of Sn-Bronze are strongly influenced by the relative motion between the solid and the liquid. In the presented paper the formation of macrosegregations in continuous casting of a columnar solidifying Sn-Bronze is studied by differentiating between 4 flow phenomena:

1. forced convection known as 'inlet jet-mush' interaction
2. solutal buoyancy driven flow
3. thermal buoyancy driven flow
4. and shrinkage-induced feeding flow

each with a high and a low Blake-Kozeny-type mush permeability.

Conclusions gained from the study of the different macrosegregation formation mechanisms can be gathered as follows:

- In the first case, where just inlet flow is considered, negative macrosegregations are predicted on the surface for both permeability values used, caused by the influence of the inlet jet on the flow field, and positive macrosegregations are predicted in the bulk of the casting. Here higher permeability leads to more pronounced macrosegregations.
- For the investigated configuration, solutal buoyancy driven flow is negligible in the case of a low permeability. Considering a higher permeability, negative segregations occur at the wall and in the middle of the casting, whereas enrichment of solute is predicted close to the solute poor region near the casting wall.
- For both permeability values used, thermal buoyancy driven flow and its interaction with the inlet jet and the mushy zone play an important rule. The negative surface macrosegregations and the positive bulk macrosegregations are more pronounced in comparison to the case where just inlet flow is considered. With a higher mush permeability the larger mushy zone enables an increase of macrosegregations throughout the whole casting.
- Shrinkage-induced feeding flow causes positive macrosegregations at the surface and negative ones in the center of the casting. In the case of a high mush permeability solute poor solid is formed at the wall, followed by a positively segregated area around negatively segregated solids in the center.
- The cases which include feeding flow, thermo-solutal buoyancy flow and forced convection show the expected superposition of the different phenomena. In the case of a lower permeability, positive macrosegregations are predicted at the wall and strong negative ones at the center line. The high permeability in Case E-H causes significant changes in the macrosegregation pattern, namely negative segregations at the wall (caused by the inlet jet) and at the center line (mainly influenced by feeding flow), while for the rest, positive macrosegregations are predicted.

The results show the high dependence of macrosegregations on the flow pattern and hence on the permeability of the mushy zone. Generally, it can be stated that higher permeability increases the possibility of fluid movement in the mushy zone which goes hand in hand with more pronounced macrosegregations in the casting.

In further investigations it is planned to include the nucleation of equiaxed grains, which will influence the formation of macrosegregations significantly in addition to the discussed flow phenomena.

**Acknowledgement:** This study was financially supported by the Austria Christian-Doppler Society (CDG) and by Wieland-Werke in Germany, which the authors thankfully acknowledge. In addition, the authors acknowledge the excellent technical support of Dr. M. Pelzer and Dipl.-Ing. R. Postl from FLUENT/Germany.

## References

- Amberg G., Shiomi J.** (2005): *FDMP: Fluid Dyn. Mater. Proc.*, vol. **1**, pp. 81-96.
- Apelian D., Flemings M.C., Mehrabian R.** (1974): *Metall. Trans.*, vol. **5**, pp. 2533-2537.
- Beckermann C.** (2002): *Inter. Mater. Reviews*, vol. **47**, p.243.
- Beckermann C., Viskanta R.** (1993): *Appl. Mech. Rev.*, vol. **46**, p. 1.
- Bernard D., Nielsen  $\Phi$ ., Salvo L., Cloetens P.** (2005): *Mater. Sci. Eng.*, vol. **A392**, p.112.
- Bird R.B., Steward W.E., Lightfoot E.N.** (1960): *Transport Phenomena*, John Wiley & Sons, New York, NY.
- Flemings M. C.** (2000): *ISIJ Intern.*, vol. **40**, p.833.
- Flemings M.C., Nereo G.E.** (1967): *Trans. Metall. Society AIME* vol. **239**, pp. 1449-1460.
- Flemings M.C., Mehrabian R., Nereo G.E.** (1967): *Trans. Metall. Society AIME*, vol. **242**, pp. 41-49.
- Fluent 6.1 User's Guide** (2003): vol. 4, Fluent Inc., Lebanon, NH, USA.
- Goyeau B., Benihaddadene T., Gobin D., Quintard M.** (1999): *Metall. Mater. Trans.*, vol. **30B**, p. 613.
- Gruber-Pretzler M., Mayer F., Wu M., Ludwig A.** (2005): *Continuous Casting*, ed. H.R. Müller, Wiley-VCH, p. 219.
- Kudashov D.V., Müller H.R., Zauter R.** (2005): *Continuous Casting*, ed. H.R. Müller, Wiley-VCH, p. 256.
- Lan C. W., Yeh B. C.** (2005): *FDMP: Fluid Dyn. Mater. Proc.*, vol. **1**, pp. 33-44.
- Ludwig A., Wu M.** (2002): *Metall. Mater. Trans.*, vol. **33A**, p.3673.
- Ludwig A., Wu M.** (2005): *Mater. Sci. Eng.*, vol. **A413-414**, p.109.
- Ludwig A., Gruber-Pretzler M., Mayer F., Wu M.** (2005): *Mat. Sci. Eng.*, vol. **A413-414**, p.485.
- Miettinen J.** (2005) *Comp. Mater. Sci.*, in print.
- Nielsen  $\Phi$ ., Arnberg L., Mo A., Thevik H.** (1999): *Metall. Mater. Trans.*, vol. **30A**, p. 2455.
- Rappaz M., Thevoz Ph.** (1987): *Acta Metall.*, vol. **35**, p.1487.
- Rappaz M., Thevoz Ph.** (1987): *Acta Metall.*, vol. **35**, p.2929.
- Rappaz M., Voller V.** (1990): *Metall. Mater. Trans.*, vol. **21A**, p.749.
- Reddy A. V., Beckermann C.** (1997): *Metall. Mater. Trans.*, vol. **28B**, p.479.
- Rousset P., Rappaz M., Hannart B.** (1995): *Metall. Mater. Trans.*, vol. **26A**, p.2349.
- Schneider M., Beckermann C.** (1995): *Inter. J. Heat Mass Transfer*, vol. **38**, p.3455.
- Vreeman C. J., Krane M. J. M., Incropera F. P.** (2000): *Inter. J. Heat Mass Transfer*, vol. **43**, p.677.
- Vreeman C. J., Incropera F. P.** (2000): *Inter. J. Heat Mass Transfer*, vol. **43**, p.687.
- Voller V.R., Brent A.D., Prakash C.** (1989): *Inter. J. Heat Mass Transfer*, vol. **32**, p.1719.
- Wu M., Ludwig A., Bührig-Polaczek A., Fehlbier M., Sahm P.R.** (2003): *Inter J. Heat Mass Transfer*, vol. **46**, p.2819.
- Wu M., Ludwig A.** (2003): *Adv. Eng. Mater.*, vol. **5**, p.62.
- Wu M., Ludwig A., Pelzer M., Postl U.** (2005): *Adv. Eng. Mater.*, vol. **7**, p.846.
- Wu M., Ludwig A.** (2005): *Mater. Sci. Eng.*, vol. **A413-414**, p. 192.
- Wu M., Ludwig A.** (2006): *Metall. Mater. Trans. A*, (2006) in print.